International Communications in Heat and Mass Transfer 172 (2026) 110625

Contents lists available at ScienceDirect

International Communications in Heat and Mass Transfer

journal homepage: www.elsevier.com/locate/ichmt

Timely melting - Solidification cycles for optimizing the PCM efficiency in space

Homayoun Badfar [a], Diana C. Dubert [a,*], Jaume Massons [a], Josefina Gavaldà [a], Mounir M. Bou-Ali [b], Xavier Ruiz [a], Valentina Shevtsova [b]

[a] Universitat Rovira i Virgili, Tarragona, Spain
[b] Fluid Mechanics Group, Faculty of Engineering, Mondragon University, Mondragon, Spain

ARTICLE INFO

Keywords:
Marangoni convection
Phase change materials
Melting-solidification processes
Microgravity
2D simulations

ABSTRACT

The present study deals with a multifaceted approach to heat transfer in phase-change materials (PCM), focusing on melting - solidification full cycle of *n-Eicosane*, and applying a varying range of thermal conditions relevant to space applications. Special attention is given to the thermocapillary effect, or Marangoni convection, as it plays a critical role in the heat transfer process of PCMs under microgravity conditions. The domain proposed for the present paper is modeled having the upper surface exposed to air and the range of varying boundary conditions are imposed on the end walls. This numerical study on *n-Eicosane* complements our previous work [7], which focused on gallium. The most efficient scenario involves reversing the temperature between the cold and hot walls at key timesteps, prior to full melting or thermal equilibrium is achieved. The results show that by using a sufficient number of boundary condition switches at short time interval between them can significantly enhance the heat transfer rate, which is crucial for spacecraft applications.

1. Introduction

The phase change devices have been widely studied for thermal energy storage systems in both Earth and space applications. The literature presents many works in which their efficiency has been improved by applying different strategies such as container geometry optimization or nanoparticle enhanced PCM [1–6].

In the last years, the growing of space colonization has re-emerged the importance of optimizing the energy management in space environments by using different energy-related technologies [7,8]. PCM devices have been used for several decades in space exploration, where significant temperature fluctuations can occur [9]. As well, the PCM systems were successfully implemented in space missions for thermal regulation and environmental stabilization. Notably, they were deployed in the Soviet Venera missions to Venus to manage spacecraft temperature fluctuations [9]. Their role extends beyond Venus missions, having served as protective buffers against extreme diurnal temperature variations on planetary surfaces such as the Moon and Mars. For example, water-based PCM heat sinks have proven to be efficient in enhancing thermal management for space exploration vehicles and habitats, effectively adapting to diverse thermal loads and environmental conditions [10]. PCMs were also crucial components of the Lunar Roving Vehicle during Apollo 15, as well as Mars rovers like Sojourner, Spirit, Opportunity, Curiosity, and Perseverance [11,12]. Moreover, chalcogenide-based PCMs have been explored for spaceborne photonics applications due to their nonvolatile, reconfigurable, and fast-switching properties, along with a high degree of space radiation tolerance [13]. These advancements align with the broader utilization of PCMs in spacecraft thermal regulation, further enhancing mission reliability and efficiency across diverse space environments.

The European Space Agency (*ESA*) has expressed interest in integrating PCM technology into the future lunar infrastructure, particularly within the ESA Moon Village program, to ensure stable thermal conditions in Moon habitats despite drastic temperature shifts between lunar day and night. Studies have demonstrated that PCMs can effectively stabilize internal temperatures of habitats by absorbing and releasing latent heat during phase transitions, thereby maintaining suitable living conditions for astronauts [14,15]. This approach is particularly beneficial in microgravity or reduced gravity environments, where traditional convection-based thermal control methods are less effective.

Moreover, this study is also motivated by upcoming *MarPCM/ISS* project which aims to explore alternative methods for optimizing heat

* Corresponding author.
E-mail address: dianacristina.dubert@urv.cat (D.C. Dubert).

https://doi.org/10.1016/j.icheatmasstransfer.2026.110625

Available online 24 January 2026

management [16–18]. In particular, it explores the use of Marangoni convection as a natural mechanism to increase the heat extraction rate. This solution offers clear advantages, such as no moving parts or additional weight, making it potentially beneficial for space applications. Hence, the primary objective of the above project is to examine the dynamics of the phase change process of PCM from solid to liquid under a microgravity environment. The lack of buoyancy due to this environment, promotes the thermocapillary as the main driving force to produce convection that can enhance the melting process as reflected in the literature [7]. The study focuses particularly on investigating the impact of Marangoni flow on the melting process in cuboidal or cylindrical geometries. Various numerical approaches provide initial ground-based support for the MarPCM experiment, mainly taking into account the different flow characteristics in the melting phase for the different geometries [19–26]. Most of these analyses only consider the complete melting phase, showing that the heat extraction rate drastically diminishes as the melting progresses. One of them [23] deals with the complete melting/solidification/melting cycle. In a recent study [7] our group has carried out specific analysis of the feasibility and effectiveness of different recovery strategies for phase change materials through the complete cycle using a periodic switching of the thermal boundary conditions on the hot/cold faces. An evaluation of the rate of heat transfer were investigated under three different scenarios for a low Prandtl material, *Gallium* $Pr = 0.02$.

Results showed that a correct selection of the cycling can greatly increase the performance of the process by taking advantage of the large heat transfer rate occurring in the first stages of the melting process. This will improve the heat extraction in closed environments under microgravity conditions. The upcoming experiment MarPCM [17] onboard the International Space Station (*ISS*) will be conducted using *n-Eicosane* (*C20*) as PCM material. This specific paraffin fulfills several requirements for use on the ISS, including minimal volume change during phase transition, low vapor pressure, controlled thermal expansion, and low toxicity and reactivity with the container. *C20* has a Prandtl number significantly higher than *Gallium* ($Pr = 51$ in *C20*, 0.02 in *Gallium*) which was extensively studied in the literature [27–29]. In the absence of buoyancy, the variation in Prandtl number (Pr) is strongly justified, as it directly controls the competition between thermal and momentum boundary layer development during Marangoni-driven melting/solidification. The surface tension gradients of both materials are similar, which underlines that the observed differences in system response, and consequently in the effectiveness of the switching strategy, arise primarily from the contrast in Prandtl number, not from the magnitude of the Marangoni driving force itself. Therefore, under pure diffusive conditions, the melting of n-Eicosane is slowed down compared to the one of Gallium due to its low thermal conductivity.

The present paper analyses the heat transfer through a timely melting-solidification cycle interruption for *C20*, evaluating the performance of the process by switching the boundary conditions at certain timesteps. In the same time, the role of Marangoni convection in the context of heat transfer is as well discussed.

The paper is structured in several sections including the problem formulation, which deals with the governing equations used for melting/solidification cycle simulations, details the varying boundary conditions and gives a brief description of the numerical model used. The main results are presented in the following section, where the focus is directed on the evaluation of the PCM's heat transfer rate under microgravity conditions for three specific cases of boundary conditions. The latter section ends with an evaluation of the heat transfer enhancement through a coefficient of performance, followed by the main conclusions of the study.

2. Methodology and numerical simulation

2.1. Governing equations

A rectangular cell with a height of $H = 0.8$ cm and a length of $L = 6.4$ cm is used for all simulations, yielding an aspect ratio of $AR = L/H = 8$. The sketch of the system is depicted in Fig. 1.

The flow inside the numerical domain is assumed to be laminar and incompressible, and with constant thermophysical properties (see Table 1). PCM in liquid form is assumed to behave as Newtonian fluid, viscous dissipation and volume expansion due to phase change are neglected, and weightless conditions ($g = 0$) are assumed. The system dynamics is governed by the momentum and continuity equations:

$$\partial_t u + (u \bullet \nabla)u = -\frac{1}{\rho_0}\nabla p + \nu\nabla^2 u + \frac{1}{\rho_0}DS \tag{1}$$

$$\nabla \bullet u = 0 \tag{2}$$

where $u = (u_x, u_y)$ is the velocity vector, p is the buoyant pressure, ρ_0 is the reference density, and $\nu = \mu/\rho_0$ is the kinematic viscosity.

The DS term in the momentum equation Eq. (1) models the solid-liquid transition using the Carman-Kozeny approach, by treating the interface as a porous mushy layer where both phases coexist [5]. This allows solving a single momentum equation for both solid and liquid phases, with the solid phase remaining stationary:

$$DS = \frac{C(1-l_f)^2}{l_f^3 + b}u \tag{3}$$

where l_f represents the local liquid fraction, serving as the link between the momentum and energy equations. It varies from 0 (solid) to 1 (liquid), with intermediate values in the mushy region where the phases mix. Since the liquid fraction is not precisely defined in this region, it is typically approximated by using a linear interpolation between the solidus (T_s) and liquidus (T_m) temperatures:

$$l_f = \begin{cases} 0 & T \le T_s, \\ 1 & T \ge T_m, \\ \dfrac{T - T_s}{T_m - T_s} & T_s < T < T_m. \end{cases} \tag{4}$$

Following previous studies [24,25,31,32], the parameter values in Eq. (3) are set as $C = 1.6 \times 10^6$ kg m^3 s to characterize permeability, while $b = 10^{-3}$ prevents division by zero when $l_f = 0$. The energy equation considers both heat transfer and the phase change, with the latent heat of fusion, L_f, defined as follows:

$$\rho_0 c_p \left(\frac{\partial T}{\partial t} + u \bullet \nabla T\right) = \nabla^2(kT) - \rho_0 L_f \frac{\partial l_f}{\partial t} \tag{5}$$

where k and c_p are the thermal conductivity and specific heat weighted between liquid and solid phase according to:

$$(c_p, k) = (c_{ps}, k_s)(1 - l_f) + (c_{pl}, k_l)l_f \tag{6}$$

2.2. Imposed conditions at the end-walls

No-slip conditions are imposed on all boundaries except for the top wall, which is set as a free surface to allow Marangoni convection to occur. The top and bottom walls are treated as adiabatic, whereas the lateral walls are kept at constant temperatures, yet different values. These temperature settings are analyzed in relation to various approaches for the melting and solidification processes. Initially, the PCM is in a solid state with a uniform temperature below the melting point, set at $T_s = T_m - 1$ K. The melting process begins when a temperature of $T_m + \Delta T$, $\Delta T = 40$ K, is applied at the left wall, while the right wall's temperature is set at T_m (see Fig. 2, *Cases 1 and 2*). Once the system

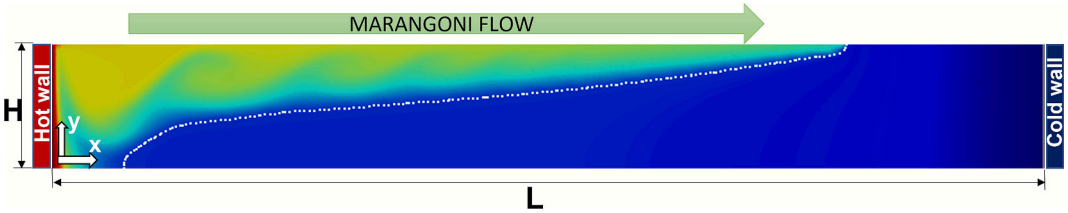

Fig. 1. Sketch of the numerical domain used for simulation.

Table 1
Thermophysical properties of n-eicosane [16,21,30].

Property	Symbol	Liquid phase	Solid phase
Density (kg/m^3)	ρ_0	775	
Dynamic viscosity (kg/m s)	μ	0.00326	–
Thermal conductivity (W/m K)	k_l/k_s	0.149	0.385
Thermal diffusivity (m^2/s)	α_l/α_s	8.2×10^{-8}	2.67×10^{-7}
Specific heat (J/kg K)	$c_{p,l}/c_{p,s}$	2280	2000
Latent heat (J/kg)	L_f	247,600	–
Liquidus/solidus temperature (K)	T_l/T_s	310.5	308.5
Surface tension gradient (N/m K)	σ_T	-9.75×10^{-5}	–
Melting temperature (K)	T_m	309.5	–
Prandtl number, Pr = ν/α	Pr	51	
Marangoni number, Ma = $\lvert\sigma_T\rvert L\Delta T/(\mu_l \alpha_l)$	Ma	9.3×10^5	

Here $\sigma_T = (d\sigma/dT)_{Tref}$ and $\alpha_l = k_l/\rho_0 c_{p,b}$ where m, l, and s stand for the melt, liquid and solid, respectively.

reaches a steady state (full melting), the solidification process is initiated by altering the boundary temperatures at either the left or right wall [32]. Regarding *Case 3*, the temperature at the left wall is kept $T_m + \Delta T$ while the right wall is set at $T_m - \Delta T$, doubling the temperature gradient considered for Case 1 and 2. The different sets of boundary conditions for melting and solidification processes are outlined in Fig. 2. Remark that, for these first two cases, the switching of the thermal boundary conditions is applied for a single PCM melting/solidification cycle, whereas in *Case 3* the switching is applied over multiple cycles at previously defined time interval. The switching of boundary conditions is done instantaneously as can be seen in Fig. 2. For the melting and solidification phases, the initial conditions are summarized in Table 2.

The temperatures imposed at the end walls generate gradients in the axial direction (parallel to the temperature gradient) that drive the Marangoni convection once the PCM begins to melt. Consequently, the boundary condition at the solid/air interface (y = H) is governed by the balance between viscous forces and thermocapillary forces:

$$\nabla_n u_t = \frac{\sigma_T}{\mu} \nabla_t T; u_n = 0 \tag{7}$$

where u_t and u_n refer to the normal and tangential velocity components of the liquid phase respectively, μ the liquid dynamic viscosity and σ_T the surface tension gradient.

To evaluate the intensity of Marangoni convection, the dimensionless Marangoni number is defined as:

$$Ma = (|\sigma_T| L \Delta T)/(\mu \alpha_l) \tag{8}$$

2.3. Numerical model

In order to solve the equations mentioned above, we have used the finite-volume software in open access OpenFOAM environment, following the approach detailed in literature [23–25]. The numerical solver employs the PIMPLE algorithm, a hybridization between SIMPLE and PISO algorithms, for pressure-velocity coupling and second-order schemes for spatial and temporal discretization [23–26]. To select the

Table 2
Overview of boundary conditions in multiple cases, for both melting and solidification phases.

Case	T(x = 0)	T(x = L)
Melting Process		
1	$T_m + \Delta T$	T_m
2	$T_m + \Delta T$	T_m
3	$T_m + \Delta T$	$T_m - \Delta T$
Solidification Process		
1	$T_m + \Delta T$	$T_m - \Delta T$
2	$T_m - \Delta T$	T_m
3	$T_m - \Delta T$	$T_m + \Delta T$

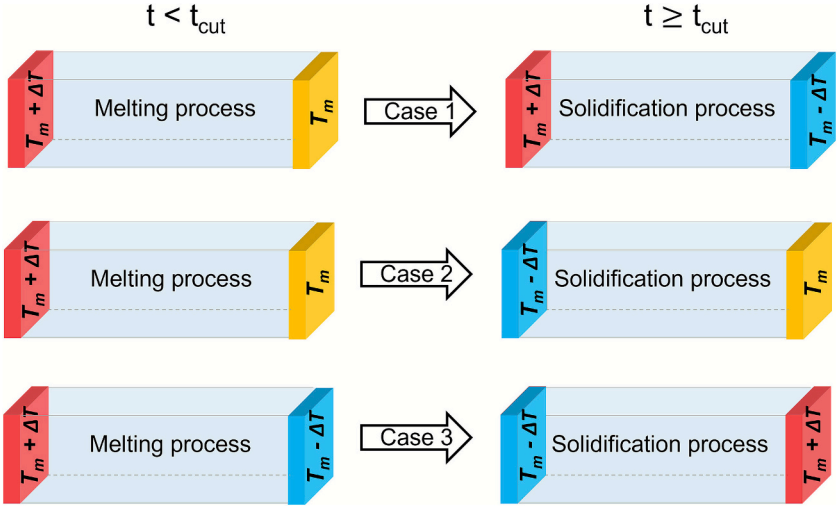

Fig. 2. Boundary conditions for melting and solidification processes for the studied cases (ΔT = 40 K).

optimum domain discretization for the present simulations, we have performed a mesh convergence test for three different meshes. The cavity was divided into 100 × 20 cells for the rough mesh, 200 × 40 cells for the medium and 400 × 80 cells in case of the fine mesh. The time step was kept constant in all simulations at $\Delta t = 0.001$ s to ensure numerical stability. The convergence test was performed for *Cases* 1 and 2 and considering only the melting stage, $t < t_{cut}$. Fig. 3 compares the time evolution of the liquid fraction and the computational runtime for the three meshes proposed.

The results identify the medium mesh as optimal for the present study as it provides a good compromise between accuracy and computational efficiency. The difference in liquid fraction evolution for medium mesh case with respect to the fine mesh scenario does not exceed 2% while in the rough mesh scenario this difference can rise up to 7%.

3. Results

In our previous paper [7], we have analyzed the above melting – solidification cycle for low Pr number PCM (*Gallium*) demonstrating that the best scenario for heat transfer enhancement is the *Case 3*. In the present work, we will detail the all three scenarios discussed previously, though applied for n-eicosane.

Heat transfer rate (Q *in W/m*) is one of the key characteristics of PCM system performance. It is defined as the integral of the local heat flux over the height H through either the hot or cold wall, $q = -k\partial T/\partial x$,

$$Q = -\int_0^H k(\partial \mathrm{T}/\partial \mathrm{x})_{x=0,L} dy \tag{9}$$

where k is already defined in Eq. (6) as weighed averaged thermal conductivity. A positive heat transfer value implies a heat flowing in the positive x direction.

3.1. The heat transfer rate analyses for Cases 1 and 2

3.1.1. Melting process

The heat transfer rate for *C20* in the first two cases of boundary conditions and for the complete melting/solidification cycle is depicted in Fig. 4. The heat transfer rate of *n-Eicosane* at hot wall (black) and cold wall (red) are displayed for *Case 1 and 2*. Remark that, the melting subcycle for both cases coincide. The vertical black line marks the transition between melting and solidification processes.

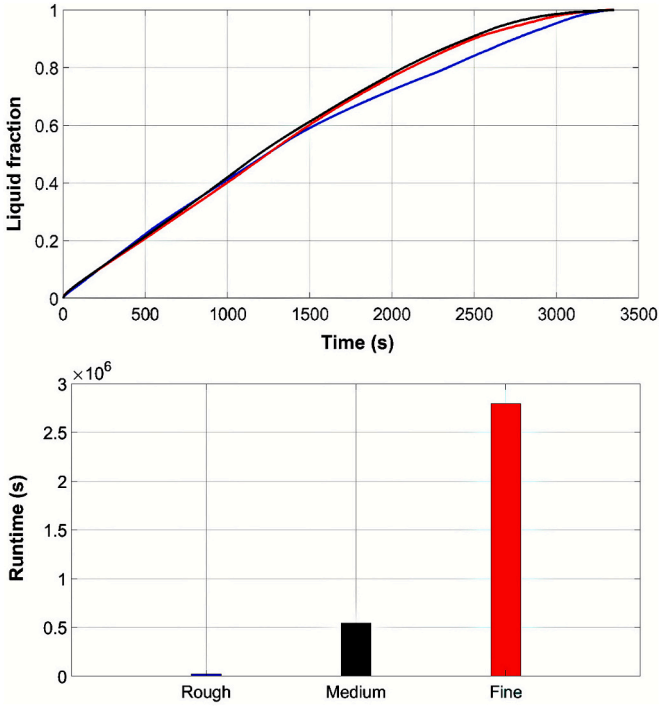

Fig. 3. Comparison of the liquid fraction evolution and runtime for the three different meshes considered for convergence test.

At the hot wall, left side of the domain ($x = 0$), the heat transfer rate (black curve) for n-eicosane initially decreased to 40 W/m within 200 s, then gradually increases, peaking at 50 W/m around 1500 s when the liquid fraction near the free interface reaches the cold wall (see Fig. 4). After 3500 s the system reaches a steady state with a stabilized heat transfer rate of 25 W/m. Calculating the heat transfer rate due to pure conduction the obtained value is around 0.74 W/m indicating that *C20* is largely influenced by Marangoni convection, which significantly enhances heat transfer rate.

At the cold wall (x = L), the material exhibits an initial weak heat transfer rate (red curve) due to low temperature gradients. At the onset (up to 1000 s) of the melting process the temperature of the PCM is below the temperature of the right wall (T_m). This will produce an incoming negative value of heat from the cold wall. As the PCM temperature increases and the liquid/solid interface nears the cold wall, the heat transfer rate abruptly turns positive, implying that heat is extracted from the wall. The heat flux smoothly increases due to the slow buildup of the liquid fraction, leading to a steady-state heat transfer rate of 25 W/m overlapping the value obtained at hot wall.

Overall, the behavior of *C20* during the melting relies predominantly on convective transport, leading to a gradual heat transfer evolution which stabilizes at a lower value compared to that of *Gallium* detected elsewhere for *Case 1* ($Q_{Gallium}$ = 240 W/m [7].

3.1.2. Solidification process

Once the complete melting at t_{cut} = 4500 s is reached, the boundary conditions change and the solidification process initiates. The temperature at the cold wall (x = L), initially being at T_m, is suddenly dropped by ΔT = 40 K, leading to a sharp decline in Q during the initial instants. This transient response relates to the fast adjustment of the thermal field as the temperature gradient steepens immediately after cold wall boundary is modified. The heat flux rapidly stabilizes around 37 W/m indicating that the system has reached a quasi-steady regime with a constant rate of heat extraction which is faster than in case of melting. As the solid layer grows and the latent heat is released the heat transfer rate at the left wall ($x = 0$), progressively evolves towards the steady value of 37 W/m.

In the *Case 2*, the boundary conditions are kept the same as in *Case 1* during melting, however for the solidification subcycle the boundary conditions at the hot wall are modified so that the temperature at the wall drops by ΔT. Therefore, the solidification direction is set from left to right. Heat transfer at $x = 0$ (blue curve) remains practically negative during the entire process, indicating a continuously heat removal from the PCM, which drives the solidification process steadily. At the right wall (x = L) the heat transfer rate (green curve) is negligible until undergoes a sign change around $t \sim$ 40,000 s as shown in Fig. 4 when the $t = \infty$ extended timescale. The sign reversal of heat flux observed at $x = L$ arises from the slow propagation of the thermal disturbance across the PCM domain after switching. Following the switch, the left wall ($x = 0$) temperature drops, initiating solidification from that side. However, due to the large aspect ratio (AR = 8) and the low thermal diffusivity of the PCM, the cold thermal wave travels slowly along the length L. Only after a time comparable to the longitudinal thermal diffusion time ($t_{ch,L} = L^2/\alpha \sim$ 50,000 s in liquid) does the temperature at the right wall ($x = L$) begin to fall significantly. Once the temperature at $x = L$ drops below the temperature $T = T_m$, the local temperature gradient reverses, leading to the observed sign change in heat flux. This delayed response highlights the importance of thermal inertia and diffusive timescales in elongated PCM systems under transient boundary conditions. In this case, Marangoni flow is largely suppressed as the liquid phase remains isothermal at $T = T_m$. The values at both walls begin to converge at approximately t

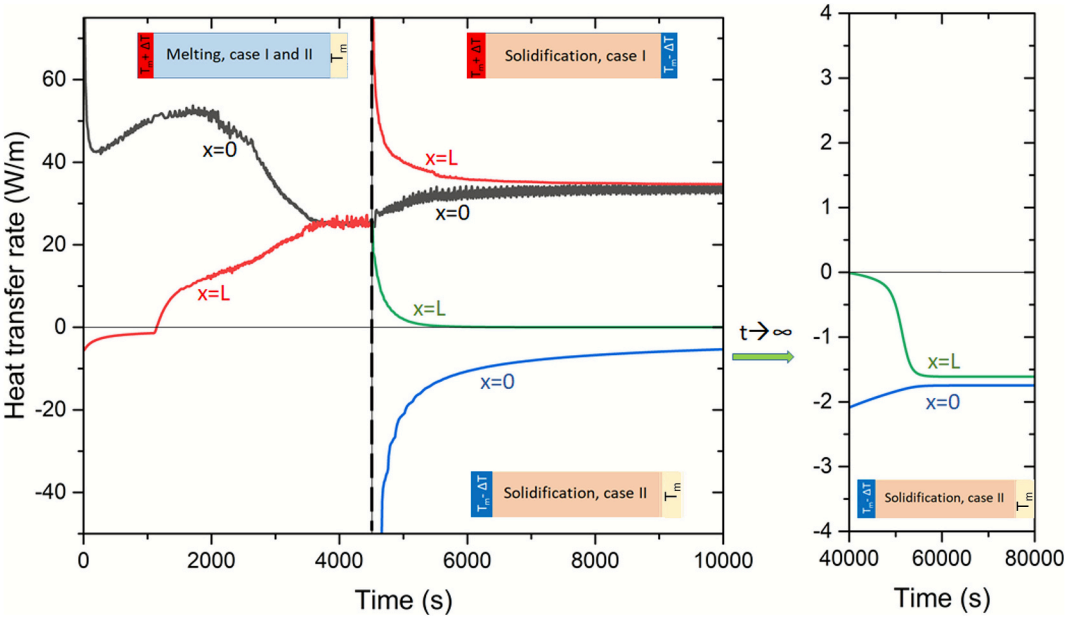

Fig. 4. Heat transfer rate of n-eicosane (*C20*) for full cycle in *Case 1 and 2*. The right - hand panel presents the asymptotic behavior at extended times for solidification process in *Case 2*.

~ 57,000 s, eventually stabilizing at $Q_{cond} = -1.75$ W/m, which corresponds to the conductive heat transfer of the solid PCM, calculated as $Q_{cond} = k_s H\Delta T / L$.

The sharp discontinuities in the heat flux curves in Fig. 4, at $t_{cut} =$ 4500 s, reflect the instantaneous nature of the boundary switch. At this moment, the thermal boundary layer is effectively reset, resulting in a steep temperature gradient that drives high initial heat transfer rates. This is followed by a gradual relaxation as the melted/solidified region evolves toward a new quasi-steady profile.

Overall, *C20*'s solidification phase unfolds over long period, with the conduction playing a dominant role in the late stages of heat transfer. Comparing to gallium [7], *C20* is around 50 times slower in heat transfer behavior, emphasizing the substantial difference in their thermal response during solidification.

3.2. Propagation of melting front in Case 1 and 2

To highlight the role of Marangoni convection in the context of heat transfer, Fig. 5 shows the snapshots of liquid/solid fractions at the selected time moments. Given that the thermal conductivity of *n-Eicosane* is relatively low, it can be seen that Marangoni convection plays an essential role. The evolution of the melting front is depicted in the left panel of Fig. 5. At first, heat transfer is dominated by conduction, leading to a uniform advancement of the melting front parallel to the hot wall. As the process evolves, thermocapillary effects induce localized convection near the interface. The initially steep temperature gradient accelerates the formation of the thin liquid layer beneath the surface. Marangoni-driven flow transports the molten material from the hotter to the cooler region, intensifying the melting process. In a relatively short period, this convective motion causes the liquid phase to expand across the solid surface, ultimately reaching the opposite wall. A comparison of the melting front topologies between *C20* and *Gallium* [7] clearly

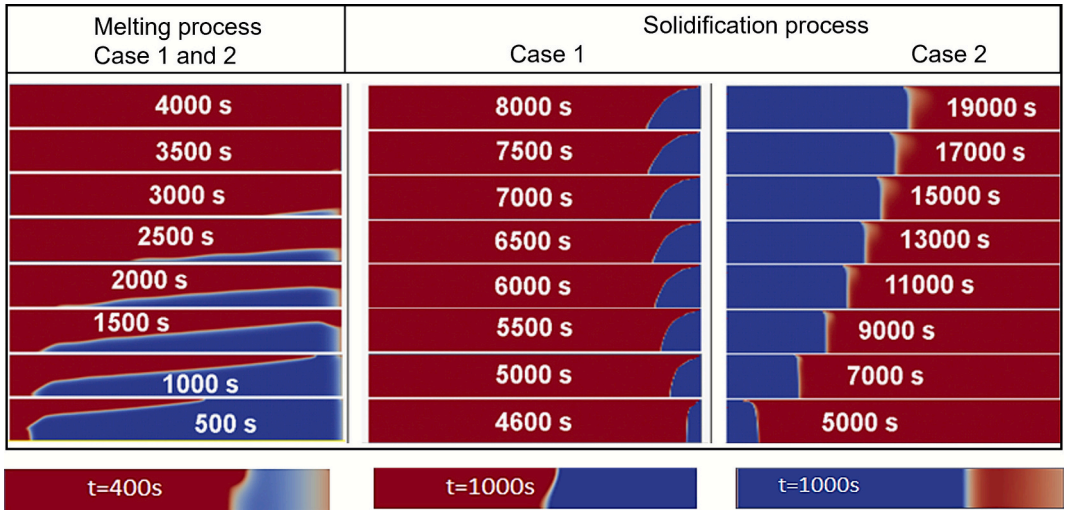

Fig. 5. Snapshots tracking the transient evolution of the solid-liquid interface during both melting and solidification of *n-Eicosane*. Red indicates liquid, while blue indicates the solid phase. The snapshots are shown at key moments rather than at equal intervals. For reference, a representative snapshot from each phase is also provided for gallium (at the bottom). (For interpretation of the references to colour in this figure legend, the reader is referred to the web version of this article.)

demonstrates that the role of the Marangoni effect in case of *n-Eicosane* is significantly greater than for *Gallium* in the melting phase (snapshot for *Gallium* located just under *C20* snapshots in Fig. 5).

In case of solidification of n-eicosane, this process is strongly influenced by Marangoni number, which is calculated based on Eq. (10) and is two orders of magnitude higher than for gallium (approximately 93)

$$M_a = \frac{|\sigma_T| L\Delta T}{\mu\alpha_l}, \frac{M_{aC20}}{M_{aGa}} \sim 93 \tag{10}$$

The central panel of Fig. 5 shows that in *Case 1*, Marangoni convection acting on the left side of the domain effectively resists the advance of the solidification front from the right side. In *Case 2*, after switching the boundary conditions, the temperature gradient is reduced to half of that in *Case 1*, leading to weaker Marangoni convection. Furthermore, the temperature along the melted region becomes nearly constant. As a result, the solidification front efficiently propagates toward the right side. The weak convection is evidenced by the nearly parallel alignment of the melting front with the wall and a slight elongation at the subsurface.

In the previous paper [7], we have developed a 1D analytical solution for each case considering only the thermal conduction (Stefan problem) ignoring the thermocapillary effect. This solution considers that both liquid and solid fractions evolve by square root of time as defined in Eqs. (11) and (12):

$$\frac{x_0}{L} = \sqrt{\frac{2k_l\Delta T}{\rho\left[L_f + 0.5c_{p,l}\Delta T + \left(c_{p,l} - c_{p,s}\right)T_m\right]L^2}t} \tag{11}$$

$$\frac{L - x_0}{L} = \sqrt{\frac{2k_s\Delta T}{\rho\left[L_f + 0.5c_{p,s}\Delta T + \left(c_{p,l} - c_{p,s}\right)T_m\right]L^2}t} \tag{12}$$

where x_0/L is the normalized distance of the melting front from the wall or the liquid fraction and $(L\text{-}x_0)/L$ represents the solid fraction. The physical properties used in Eqs. (11) and (12) are defined in Table 1. Therefore, for better visibility, we will compare the square of this quantity $((x_0/L)^2)$ calculated at given points to illustrate the linear dependency. This is plotted in Fig. 6 where we compare the results of the 1D analytical model with the numerical simulation conducted in this paper.

The thick blue and black curves show the temporal evolution of the liquid fraction values in *Case 1* and *2*, extracted from the simulations. Note that, when $t < t_{cut}$ the evolution of the liquid fraction in both cases coincide. The black square symbols represent the output of the numerical solution as $(x_0/L)^2$ for time steps $t < t_{cut}$ while the blue circles identify the squared solid fraction as $((L - x_0)/L)^2$ for $t > t_{cut}$ and for *Case 2* of boundary conditions. Regarding the thin black and blue lines, these correspond to the analytical solution obtained through the Eqs. (11) and (12). The poor agreement between the symbols and the thin straight lines indicate that thermal conduction is insignificant highlighting once more the relevance of the Marangoni effect during the melting.

During the process' second phase (solidification – right side of the Fig. 6, the behavior for *Cases 1* and *2* differs. For *Case 1* (represented by the thick black curve), the liquid fraction quickly stabilizes at $x_0/L \sim 0.88$. To quantify the importance of Marangoni convection over conduction, a simple theoretical model, equaling the conductive heat flux in both solid and liquid phases, has been used to determine the position of the liquid/solid front in the steady state. The predicted value ($x_0/L \sim 0.3$) is considerably lower than the value obtained in the simulations ($x_0/L \sim 0.88$), confirming the importance of Marangoni convection. For *Case 2* (thick blue curve), the process is much slower than in the previous case. When convection is nearly absent, the results of the simulations better match those predicted by the 1D model. The blue symbols representing $((L\text{-}x_0)/L)^2$ exhibit a linear tendency with a slope that agrees reasonably well with that of the analytical model (see Eq. (12)), shown by the thin blue line with a slope of $m = 18.6 \times 10^{-6}$ s^{-1}. By

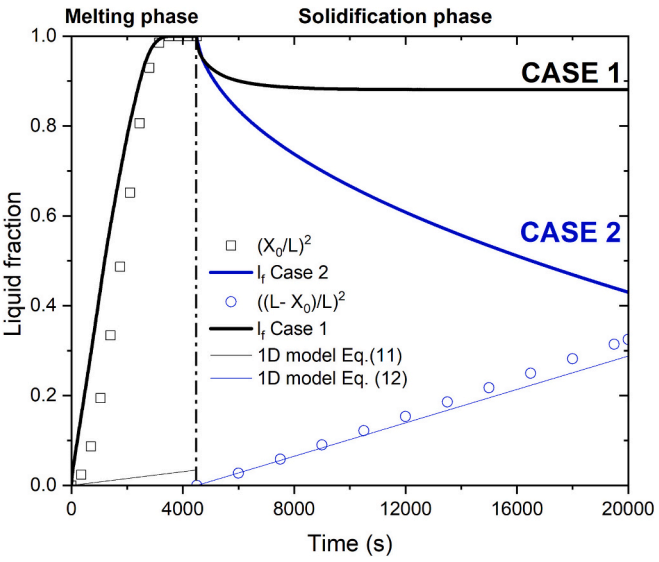

Fig. 6. Evolution of the liquid fraction for *Cases 1* and *2* for *C20*. The thick lines represent numerical simulations of the liquid fraction. Black and blue symbols show the position of the melting front as $(x_0/L)^2$ and $((L - x_0)/L)^2$ calculated at given points for *Cases 1 and 2*, respectively. This is compared with 1D analytical model shown by the thin black and blue lines, without considering the Marangoni effect. The inset shows a zoom focused on the first instants of the process. The dashed vertical line separates the melting and solidification phases. (For interpretation of the references to colour in this figure legend, the reader is referred to the web version of this article.)

extrapolating this line, we can predict that the complete solidification will occur at $t = 1/m \sim 54{,}000$ s after the freezing of the left side of the PCM box, so at $t = 54{,}000 + 4500 = 58{,}500$ s. This value agrees with the time in which the heat transfer reaches stationary state (see Fig. 4 extended times).

3.3. Case 3 switching of boundary conditions

A detailed overview of the *Case 3* scenario including the temperature reversal at selected times is presented in Fig. 7. The left wall temperature remains fixed at $T_m + \Delta T$, while the right wall is initially set to $T_m - \Delta T$, doubling the temperature gradient to $2\Delta T/L$ (see Fig. 2). It can be noticed that, the first boundary switch is completed at the $t_{cut} = 3350$ s, approximately coinciding with the finalization of the melting process. Beyond this point, the reversal of the boundaries is performed at $t_{cut} = 3950$ s and $t_{cut} = 4550$ s, setting a periodic temperature inversion every $t_s = 600$ s. This temperature switch creates a symmetric thermal boundary condition that optimize the heat transfer. The present configuration represents a multi-cycle configuration and has been previously analyzed by the authors for *n-Eicosane* [7], so just the key results are summarized herein.

Fig. 8 plots the temporal evolution of the extracted heat under these multi-cycle boundary conditions, where the wall temperatures are inverted periodically.

The upper left inset recalls the previously analyzed heat transfer rate at both $x = 0$ and $x = L$ for *n-Eicosane* and $t_s = 1000$ s [7]. In the present paper we have complemented the analysis of the switching scenarios with another $t_s = 600$ s which is represented in Fig. 8 lower right inset. Initially, the heat flux at the hot wall ($x = 0$) drops to 60 W/m within 200 s, then gradually increases peaking at 68 W/m around 2000 s. Then, the heat flux diminishes once more, reaching the steady state at 48 W/m after approximately 3350 s. At this time, $t_{cut} = 3350$ s, the boundaries are inverted each 600 s, allowing a cyclic phase transition that enhances heat flux by leveraging latent heat. By periodically inverting the temperature the solid phase repeatedly contacts the hot plate while the

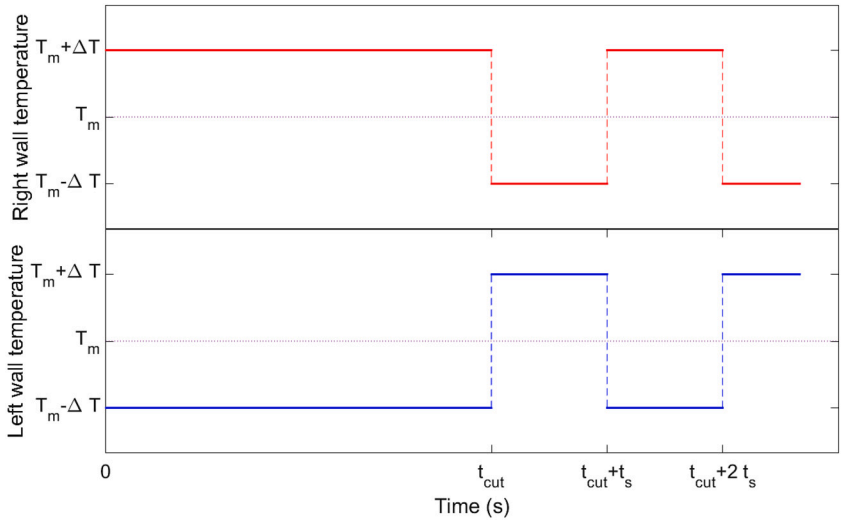

Fig. 7. Detailed sketch of the end walls temperature periodic reversal every $t_s = 600$ (s) for *Case 3* scenario.

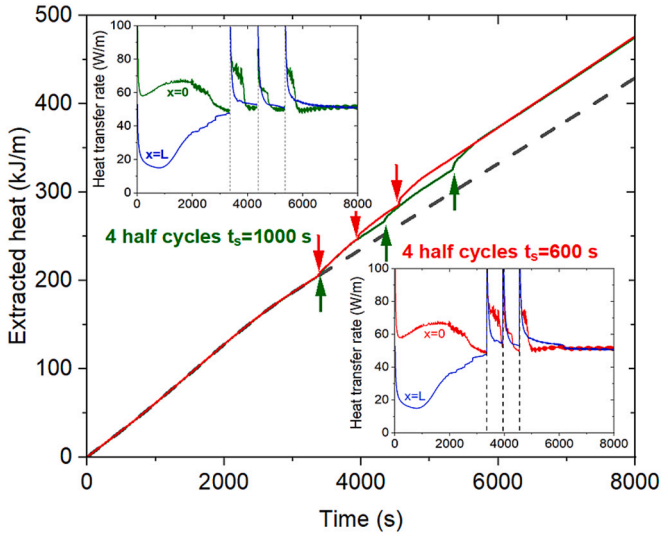

Fig. 8. Temporal evolution of heat extraction (red and green central lines) under multi-cycle conditions for *n-Eicosane*. The black dashed line represents the heat extraction if no switching is adopted. Insets: temporal evolution of the heat transfer rate at $x = 0$ (hot wall) and at $x = L$ (cold wall) during periodic change of the wall temperatures each $t_s = 600$ s and $t_s = 1000$ s. The red and green arrows indicate the time instants corresponding to each rotation of the boundaries. (For interpretation of the references to colour in this figure legend, the reader is referred to the web version of this article.)

liquid phase meets the cold plate. This strategy produces a sharp increase in the heat power extracted from the hot source in the early moments of the process.

During melting, the heat transfer rate at the cold wall ($x = L$) is initially lower than at the hot wall ($x = 0$), although both converge at steady state value of 48 W/m. However, once the melting process repeats, this difference reduces, as shown by the similarity of the red and blue curves at $t_{cuts} > 3350$ s in Fig. 8, inset. This power then, falls rapidly, converging to a final stationary state, that is broken by the next temperature inversion. After completing the last half cycle at $t = 4550$ s, a steady state is rapidly achieved. The duration of the latter half cycle is extended to 8000 s to illustrate the oscillatory behavior when the system stabilizes.

The amount of heat extracted from the hot area (x = 0) was obtained by integrating the heat transfer rate over the surface. The black dashed curve corresponds to the process with a single thermal cycle, without rotation, therefore, the boundary conditions are kept unchanged. As the heat flux rate after $t_{cut} = 3350$ s stabilizes at 48 W/m, the extracted heat evolves linearly. The comparison between the heat extracted under multi-cycle boundary conditions (red and green lines) and the single-cycle case (black dashed line) clearly demonstrates the advantage of periodically alternating the wall temperatures. This is due to the fact that, after each rotation of the boundaries a sharp increase in the power extracted is observed for both $x = 0$ and $x = L$ surfaces.

Implementing this approach requires reversing the heat transfer direction, which poses practical challenges. To circumvent this inconvenience, the authors propose rotating the PCM body (the cell without walls) by 180^0 at t_{cut}, while maintaining fixed the wall temperatures, as illustrated in Fig. 9. This rotation strategy simplifies the system design and operation. To further illustrate the concept, we provide a supplementary animation, Switch.gif.

3.4. Evaluation of the heat transfer enhancement

The effectiveness of the *Case 3* temperature-switching strategy relies on symmetric thermal boundary conditions that is greatly affected by the time intervals between two consecutive switching and the number of cycles. The switching intervals $t_s = 600$ s and 1000s were chosen to cover the characteristic melting–solidification timescale of n-eicosane under the given boundary conditions, allowing us to study the system response near and beyond the thermal relaxation time ($\tau = H^2/\alpha$). The thermal time at height H (shortest distance) for solid phase $\tau \sim 240$ s and for liquid $\tau \sim 780$ s.

In case of the four cycles analyzed, a sudden increase in the extracted

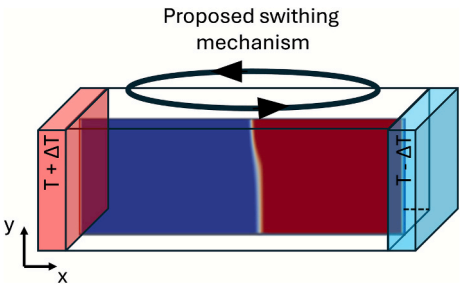

Fig. 9. Proposed practical implementation: a switching mechanism that rotates the PCM-containing cell while maintaining constant external wall temperatures.

heat is observed at each t_s (see Fig. 8 red and green arrows) which later on stabilizes at 48 W/m likewise without switching case. Despite, the t_s = 600 s case generates a slight increase in the heat extracted compared to the t_s = 1000s, their long-term values overlap. This situation yields an increase in the overall heat extracted of about 13% compared to the non-rotational boundaries case. This percentage is slightly affected by the reduction of switching intervals, although, is highly dependent on the number of cycles applied. The increase in the number of cycles produces a major divergence between the red and green lines (heat extraction during several switching) and the dashed line (without switching) in Fig. 8. This divergence reflects the cumulative enhancement in the heat extraction as the number of switches increases, suggesting that the optimal scenario is achieved when a large enough number of switching cycles is employed.

We note that, due to the periodic inversion of the thermal boundary conditions, the system never reaches a truly steady or quasi-steady regime during any part of the melting–solidification cycle. As a consequence, classical time-averaged heat-transfer coefficients defined over a cycle are not uniquely defined and depend on the selected time window and on the phase of the cycle in which the averaging is performed. For this reason, we base our analysis on quantities that remain invariant under cyclic boundary switching, namely, the integrated heat extracted per half-cycle and the Coefficient of Performance (CoP) defined by equation in Fig. 10, which more directly capture the actual heat-extraction capability of the system.

The CoP is calculated as the gain of extracted heat only for the second half cycle (1st switch), assuming that it is representative of all the others. Fig. 10 shows the dependence of the *CoP* on the switching interval, t_s, between consecutive switches. To clarify the calculation method, the inset shows the heat transfer rate when only one rotation is applied directly after the time t_{cut}. For each t_s, the *CoP* is determined as the ratio between the heat extracted during t_s, (shaded red area) and the heat that would be extracted if no rotation is considered (the area below the blue line). In the latter case the $CoP = 48 * t_s$, since $Q = 48$ W/m when the steady state is reached at t_{cut}. The *CoP* was determined for t_s in the range 100 - 1200 s considering a timestep of 1 s (solid line). As expected, the performance coefficient increases as switching time decreases. For large values of t_s, the *CoP* tends to the unity, indicating that there is no gain in the long-term efficiency when an extremely long cycle is used. The inflection point of the *CoP*, which occurs at about $t_s = 500$ s, reflects the change in the shape of heat transfer rate curve that suddenly drops

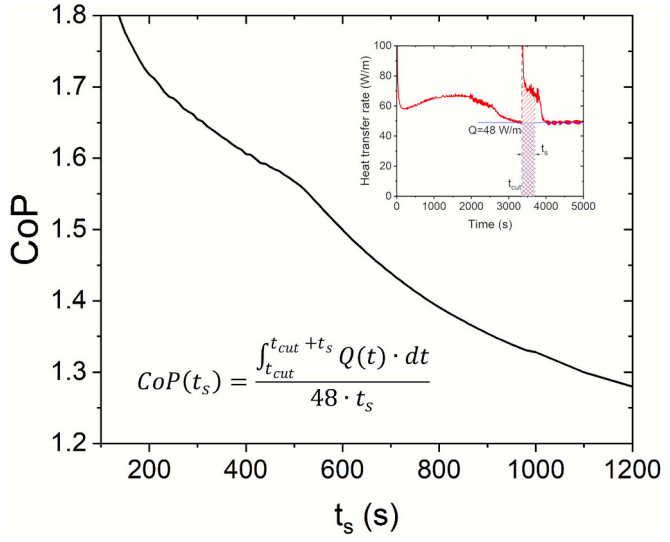

Fig. 10. Evolution of the Coefficient of Performance (*CoP*) as a function of the time period between switches (t_s). The inset shows the heat transfer rate, Q, extracted from the hot side ($x = 0$) in a process with two switches starting from t_{cut} = 3350 s. The equation details the calculation of the *CoP*.

around this moment. For a sufficiently large number of cycles with a switching time of $t_s = 600$ s, the value of *CoP* is around 1.5, indicating a 50% gain in efficiency compared to a non-rotating configuration. For t_s = 1000 s, the *CoP* is reduced to 1.3.

The monotonic increase in CoP with decreasing t_s, from 1.3 at t_s = 1200 s to 2.0 at t_s = 100 s, indicates that shorter switching periods generally yield higher efficiency gains, provided mechanical and operational constraints allow it. This trend provides a scalable principle for optimizing PCM-based thermal systems over a range of operating conditions

4. Conclusions

We have examined the heat transfer rates in the Phase Change Material, n-eicosane (*C20*), throughout complete solid-liquid-solid conversion cycles. The *n-Eicosane* has been selected as PCM material for the present study based on its proposal for the upcoming experiment MarPCM onboard the International Space Station. Building on our earlier work with gallium [7], this study extends the analysis to multi-cycle switching strategies and introduces a new performance metric, the Coefficient of Performance (CoP), to quantify efficiency gains under periodic boundary rotation. The novelty of our study lies in its comprehensive investigation of multi-cycle temperature switching, considering both melting and solidification phases at various boundary configurations, and in its practical assessment of a rotation-based implementation under Marangoni-driven convection.

Among the examined cases, the *Case 3*, with symmetric boundary conditions and multi-cyclic temperature inversion, turned out to be the most advantageous, significantly enhancing overall heat extraction efficiency. We have carefully analyzed the influence of the time intervals between switches t_s and the number of switches on the heat extraction rate. The results showed that for a limited number of switches, the performance increases, but only moderately, for example a 13% increase for a four-switch system. Increasing the number of switches the efficiency will increase. The performance gain is strongly sensitive to the switching period t_s. Shorter intervals (t_s = 100 s) yield a CoP up to 2, whereas longer intervals (t_s = 1200 s) approach CoP ≈ 1.3, indicating diminishing returns. This provides a clear compromise for system designers: higher frequency switching improves performance but may increase mechanical complexity and the energy cost for rotation. The proposed rotation-based switching mechanism, where the PCM is rotated within a fixed-temperature enclosure, offers a technologically feasible way to implement the optimized thermal cycling without active heating/cooling of walls. This approach could reduce system complexity, improve reliability, and enhance the thermal performance of PCM-based systems in microgravity environments, such as those planned for space-based thermal energy storage.

The results provide design guidelines, optimal switching times and cycle counts, which can inform the development of more efficient thermal storage and control systems for future space missions. Future studies could extend this work by exploring a range of aspect ratios and switching protocols to further generalize the optimization of PCM-based thermal systems for space applications.

CRediT authorship contribution statement

Homayoun Badfar: Writing – original draft, Software, Investigation. **Diana C. Dubert:** Writing – review & editing, Supervision, Software, Investigation, Conceptualization. **Jaume Massons:** Writing – review & editing, Writing – original draft, Investigation. **Josefina Gavaldà:** Writing – review & editing, Investigation, Funding acquisition. **Mounir M. Bou-Ali:** Writing – original draft, Funding acquisition. **Xavier Ruiz:** Writing – review & editing, Methodology, Investigation. **Valentina Shevtsova:** Writing – review & editing, Writing – original draft, Supervision.

Declaration of competing interest

The authors declare that they have no known competing financial interests or personal relationships that could have appeared to influence the work reported in this paper.

Acknowledgments

This work is supported by the following grants: PID2023-149539NB-C32 (MICINN/FEDER), PCI2024-155034-02 (MCINN/AEI) of the Spanish Government, 2023PFR-URV-00148 (Rovira i Virgili University). MMB and VS acknowledge the Basque Government for funding the MMASINT project (KK342 2023/00041, Elkartek Programme) and the Research Group Programme (IT1505- 22) and the Spanish Government for the PID2023-149539NB-C33 and PCI2024- 155071-2 projects, funded by (MICINN/FEDER) and (MCIN/AEI) respectively.

Data availability

Data will be made available on request.

References

[1] Kachalov A. Borshchak, Sánchez P. Salgado, J. Fernández, K. Olfe, Enhancing the melting of phase change materials via convective flows and container geometry, Int. Commun. Heat Mass Transfer 158 (2024) 107922. ISSN 0735-1933, https://doi.org/10.1016/j.icheatmasstransfer.2024.107922.

[2] B. Kiyak, N. Biswas, H.F. Öztop, F. Selimefendigil, Geometry curvature influence on melting and solidification performance in nano particle added phase change material to storage energy, J. Energy Storage 117 (2025) 116172. ISSN 2352-152X, https://doi.org/10.1016/j.est.2025.116172.

[3] B. Kiyak, H.F. Oztop, N. Biswas, F. Selimefendigil, Effects of geometrical configurations on melting and solidification processes in phase change materials, Appl. Therm. Eng. 258 (Part C) (2025) 124726. ISSN 1359-4311, https://doi.org/10.1016/j.applthermaleng.2024.124726.

[4] B. Kiyak, H. Fehmi Oztop, Gökhan Aksoy I, A numerical study on the effects of inclination angle and container material on thermal energy storage by phase change material in a thick-walled disc, Int. J. Numer. Methods Heat Fluid Flow 34 (3) (2023) 1227–1247. ISSN 0961-5539, https://doi.org/10.1108/HFF-07-2023-0367.

[5] S. Madruga, C. Mendoza, Enhancement of heat transfer rate on phase change materials with thermocapillary flows, Eur. Phys. J. Spec. Topics 226 (2017) 1169–1176.

[6] B. Kıyak, H.F. Öztop, Optimizing of partial porous structure for efficient heat transfer and thermal energy storage of phase change material in a rectangular cavity, J. Therm. Anal. Calorim. 149 (2024) 13425–13441, https://doi.org/10.1007/s10973-024-13634-2.

[7] D. Dubert, B. Seta, J. Massons, et al., Enhancing PCM thermal management in multi-cycle melting-solidification, Int. Comm. Heat Mass Transfer 157 (2024) 107741.

[8] Pombo D. Vázquez, A hybrid power system for a permanent colony on Mars, AAAS Space (2021) 16, 9820546.

[9] J. Collette, P. Rochus, R. Peyrou-Lauga, et al., Phase change material device for spacecraft thermal control, in: 62nd International Astronautical Congress, Cape Town, South Africa, 2011. IAC–11.C2.8.1.

[10] G. Quinn, E. Hodgson, R. Stephan, Phase change material trade study: a comparison between wax and water for manned spacecraft, in: 41st International Conference on Environmental Systems, 2011, p. 5229.

[11] S. Morea, The lunar roving vehicle: historical perspective, in: Proc. The second Conference on Lunar Bases and Space Activities of the 21st Century, Houston, TX, USA, 5-7 April 1988 2, 1988, pp. 619–632.

[12] Theodore D. Swanson, Gajanana C. Birur, NASA thermal control technologies for robotic spacecraft, Appl. Therm. Eng. 23 (9) (2003) 1055–1065, https://doi.org/10.1016/S1359-4311(03)00036-X. ISSN 1359-4311.

[13] H.J. Kim, M. Julian, C. Williams, D. Bombara, J. Hu, T. Gu, K. Aryana, G. Sauti, W. Humphreys, Versatile spaceborne photonics with chalcogenide phase-change materials, NPJ Microgravity 10 (1) (2024 Feb 20) 20, https://doi.org/10.1038/s41526-024-00358-8.

[14] Kachalov A. Borshchak, Sánchez P. Salgado, U. Martínez, J. Ezquerro, Preliminary design of a space habitat thermally controlled using phase change materials, Thermo 3 (2023) 232–247.

[15] C. Ongil, U. Martínez, Sánchez P. Salgado, Kachalov A. Borshchak, J.M. Ezquerro, K. Olfe, Laboratory experiments on passive thermal control of space habitats using phase-change materials, Thermo (2024) 4.

[16] C. Vélez, M. Khayet, J. Ortiz de Zárate, Temperature-dependent thermal properties of solid/liquid phase change even-numbered n-alkanes: n-Hexadecane, n-octadecane and n-eicosane, Appl. Energy 143 (2015) 383–394.

[17] J. Porter, A. Laverón-Simavilla, M. Bou-Ali, et al., The effect of Marangoni convection on heat transfer in phase change materials experiment, Acta Astronaut. 210 (2023) 212–223.

[18] S. Madruga, C. Mendoza, Scaling Laws During Melting Driven by Thermocapillarity 163, 2020, p. 120462.

[19] Sánchez P. Salgado, J.M. Ezquerro, J. Fernández, J. Rodríguez, Thermocapillary Effects During the Melting of Phase-change Materials in Microgravity: Steady and Oscillatory Flow Regimes 908, 2021, p. A20.

[20] Sánchez P. Salgado, J. Porter, J.M. Ezquerro, I. Tinao, A. Laverón-Simavilla, Pattern selection for thermocapillary flow in rectangular containers in microgravity, Phys. Rev. Fluids 5 (2022), 7:053502.

[21] N. García-Acosta, Sánchez P. Salgado, J. Jiménez, U. Martínez, J. Ezquerro, Thermocapillary enhanced melting of different phase-change materials in microgravity, Microgravity Sci. Technol. 34 (2022) 92.

[22] R. Varas, U. Martínez, K. Olfe, Sánchez P. Salgado, J. Porter, J. Ezquerro, Thermocapillary and natural convection during the melting of PCMs with a liquid bridge geometry, Microgravity Sci. Technol. 35 (2023) 17.

[23] B. Seta, D. Dubert, J. Massons, J. Gavaldà, M.M. Bou-Ali, X. Ruiz, Effect of Marangoni Induced Instabilities on a Melting Bridge Under Microgravity Conditions 179, 2021, p. 121665.

[24] B. Seta, D. Dubert, M. Prats, et al., Transitions between nonlinear regimes in melting and liquid bridges in microgravity, Int. J. Heat Mass Transfer 193 (2022) 122984.

[25] B. Seta, D. Dubert, J. Gavaldà, et al., Effect of heat transfer through an interface on convective melting dynamics of phase change materials, J. Fluid Mech. 966 (2023) A46, https://doi.org/10.1017/jfm.2023.463.

[26] B. Seta, Sánchez P. Salgado, D. Dubert, et al., Three-dimensional effects during thermocapillary-driven melting of PCMs in cuboidal containers in microgravity, Int. Comm. Heat Mass Transfer 150 (2024) 107198.

[27] A.D. Brent, V.R. Voller, K.J. Reid, Enthalpy-porosity technique for modeling convection-diffusion phase change: application to the melting of a pure metal, Numer. Heat Transfer 13 (1988) 297–318.

[28] F. Stella, M. Giangi, Melting of a pure metal on a vertical wall: numerical simulation, Numer. Heat Transfer A 38 (2000) 193–208.

[29] N. Hannoun, V. Alexiades, T.Z. Mai, Resolving the controversy over tin and gallium melting in a rectangular cavity heated from the side, Numer. Heat Transf. B Fundam. 44 (2003) 253–276.

[30] A. Sanjuan, B. Seta, J. Gavaldà, X. Ruiz, V. Shevtsova, M. Bou-Ali, Comparative experimental-numerical analysis of PCM: n-hexadecane, n-octadecane and n-eicosane, in: In: 27th ELGRA Biennial Symposium & General Assembly, 2022, pp. 68–69. Lisbon (Portugal).

[31] P. Egolf, H. Manz, Theory and modeling of phase change materials with and without mushy regions, Int. J. Heat Mass Transf. 37 (1994) 2917–2924.

[32] D. Dubert, B. Seta, M. Simón, et al., The melting-solidification cycle for materials with different Prandtl numbers, in: Proc. 15th Int. Meeting of Thermodiffusion (IMT15), 2023, pp. 606–614.